

Comprehensive Enumeration of Three-Dimensional Photonic Crystals Enabled through Deep Learning Assisted Fourier Synthesis

Congcong Cui,¹ Guangfeng Wei,¹ Matthias Saba^{2,3} and Lu Han^{1,}*

¹School of Chemical Science and Engineering, Tongji University, 1239 Siping Road, Shanghai, China, 200092, P. R. China

²Adolphe Merkle Institute, University of Fribourg, Chemin des Verdiers 4, CH-1700 Fribourg, Switzerland

³NCCR Bio-inspired Materials, University of Fribourg, Chemin des Verdiers 4, CH-1700 Fribourg, Switzerland

*E-mail: luhan@tongji.edu.cn

Keywords: Photonic crystal; Complete photonic bandgap; Fourier synthesis; Deep learning; Inverse design

Abstract

Three-dimensional (3D) photonic structures enable numerous applications through their unique ability to guide, trap, and manipulate light. Constructing new functional photonic crystals remains a significant challenge since traditional design principles based on band structure calculations require numerous time-consuming computations. Additionally, traditional design is based on enumerated structures making it difficult to find novel functional geometries. Here, we propose an ultra-fast photonic crystal performance prediction method to enable efficient structure optimization of arbitrary 3D photonic crystals even with multiple variable modulation. Our methodology combines Fourier synthesis — enabling the creation of any smooth geometry within a crystallographic space group — with deep learning, which facilitates efficient photonic characterization within the vast parameter space. Over 2 million structures can be explored within 2 hours using a mainstream desktop workstation. The ideal structures with desired band properties, such as large photonic bandgap, specific frequency ranges, etc., could be rapidly discovered. We systematically confirmed the well-documented assumption that the most significant photonic bandgaps are found in minimal surface morphologies, in which the single diamond (*dia* net) with $Fd\bar{3}m$ (227) symmetry reigns supreme among known photonic structures, followed by the chiral single gyroid (*srs* net) with $I4_132$ (214) symmetry. Additionally, a less well-known 3D photonic crystal with *lcs* topology within $Ia\bar{3}d$ (230) was rediscovered to exhibit a wide complete photonic bandgap, comparable to the diamond and the gyroid net. Our method not only validates the assumed hierarchy of photonic structures but also lays the foundation for the tailored design of functional materials and offers fresh insights into the advancement of next-generation optical devices and information technology.

1. Introduction

Photonic crystals are periodic, binary refractive index modulations that confine and control the propagation of light, which have significant implications for optical applications such as inhibiting spontaneous emission, guiding and bending of light, optical computers and information devices, etc.¹⁻⁴ The properties of optical materials are strongly tied to their structure. Therefore, exploring and optimizing the structure of three-dimensional (3D) photonic crystals with omnidirectional complete photonic bandgap (CPB) is a key ingredient in breaking through the current performance limitations of optical devices.⁵⁻⁸ Conventional approaches to designing photonic structures are generally based on a modulation of known structures. This includes changing the position of the dielectric interface, for example parametrized through nodal (or level set) surfaces,^{6,9,10} adding or shifting basic structural units (spheres, cylinders, etc.) at certain coordinates,^{5,11-13} modifying topology and connectivity of structural units by adding or removing material,¹⁴⁻¹⁶ searching crystallographic databases,⁷ etc. However, these methods are generally applicable to known structural types only. Designing 3D photonic crystals with unexplored crystallographic structure remains a formidable challenge for traditional photonic structure exploration, during which numerous structure optimization and laborious calculation steps are needed, which are tedious and time-consuming processes even with the help of supercomputers. Therefore, to date, due to the limitations of human imagination, a vast number of 3D symmetrical structures remain unexplored, leaving a tremendous design space for photonic structures. Another systematic approach is to formulate the problem as an objective function by appropriate mathematical methods and then generate the structure by topology optimization in a structural design region divided into pixel or voxel grids to achieve the desired performance.¹⁷⁻²⁰ Although pixelated modelling provides maximum freedom in structural design,²⁰⁻²² it requires discretized structural parameters for each pixel, and the computational requirements grow exponentially with the number of pixels.^{23,24} The remaining unexplored

structures are, therefore, a treasure trove of potential for optical applications. However, a structural design method that can describe all of them simultaneously is still elusive.

We here introduce such a method by combining a Fourier representation of possible geometries with deep learning. All 3D crystal structures can be classified into 230 space groups according to different combinations of point and translation symmetries.²⁵ Any binary, smooth crystal structure can be represented by a periodic function, calculated by an inverse Fourier transformation through the linear superposition of a series of simple trigonometric functions associated with the space group symmetries. This basic mathematical statement leads to the most versatile and topologically complex 3D morphologies. This process is also known as Fourier synthesis which is a generalized method for representing periodic functions based on Fourier series and is widely used in crystallography to determine unknown crystal structures.²⁶ Its significance has first been discussed in the context of X-ray scattering and the associated spatial electron density distribution.²⁷ The Fourier coefficients are determined by measuring the crystal structure factors through X-ray scattering experiments and phase fitting. On this basis, the crystal structures in real space can be reconstructed by calculating the electron density $\rho(r)$ of each fractional coordinate $r \in [0,1)^3$ in the unit cell to construct the level set^{28,29}

$$\rho(r) = \frac{1}{V_c} \sum_{k \in M} F_k \exp(-2\pi i k \cdot r + \alpha_k) \quad (1)$$

where V_c is the unit cell volume, M is a subset of \mathbb{Z}^3 and represents a set of crystal faces with corresponding reflection conditions in the lattice of the given space group, F_k and α_k are the amplitude and phase of the crystal structure factors corresponding to the k Miller index Bragg reflection. By using the Fourier synthesis method to the design of photonic structures, not only more suited to describing periodic structures with smooth interfaces that are more frequent in nature, but also all possible 3D photonic crystal structures can be effectively reconstructed by changing the structural parameters through the electron density formulas related to the space group symmetry, making it an ideal model for constructing photonic structures.³⁰ With this

method, the only remaining obstacle is to establish a rapid photonic analysis method to correlate the structure parameters with their optical properties.

Therefore, we propose the design of 3D photonic crystals with specified band properties using Fourier synthesis-based free modeling combined with deep learning^{31–36} and Non-dominated Sorting Genetic Algorithm II (NSGA-II)³⁷ (**Figure 1a**). The symmetry of the space group under consideration determines a particular set of systematic extinction conditions³⁸ in the Fourier synthesis process. The 3D spatial electron density distribution is calculated with random numbers (uniformly distributed in the interval) of the amplitude and phase, and then the level set is constructed by the normalized electron density $\rho_{norm}(r)$ combined with the threshold t ,

$$\rho_{norm}(r) = \frac{\rho(r) - \rho_{min}}{\rho_{max} - \rho_{min}} > t \quad (2)$$

where t represents the isosurface threshold for determining the structure boundary which adjusts the fill fraction of the corresponding dielectric materials. Thus, the allowed amplitudes and phases of the Fourier series and the threshold t serve as structural parameters whose values can be adjusted to model arbitrary periodic photonic structures in specified space group symmetries (**Figure 1b**). The corresponding photonic band structures are obtained through electromagnetic simulation employing MIT Photonic-Bands (MPB)³⁹ with a corresponding spatial resolution of $16 \times 16 \times 16$ for the initial search and $32 \times 32 \times 32$ for the computation of specific structures. Subsequently, the deep neural network is trained using the dataset constructed of 100 000 sets of structure-performance data of selected space groups to efficiently predict the photonic band structure from the structural parameters (**Figure 1c**). Then, a deep neural network acts as a proxy model for the electromagnetic simulation process, combined with a genetic algorithm to achieve an efficient search of the structural design space and obtain the photonic crystal structural parameters with specified band characteristics (**Figure 1d**).

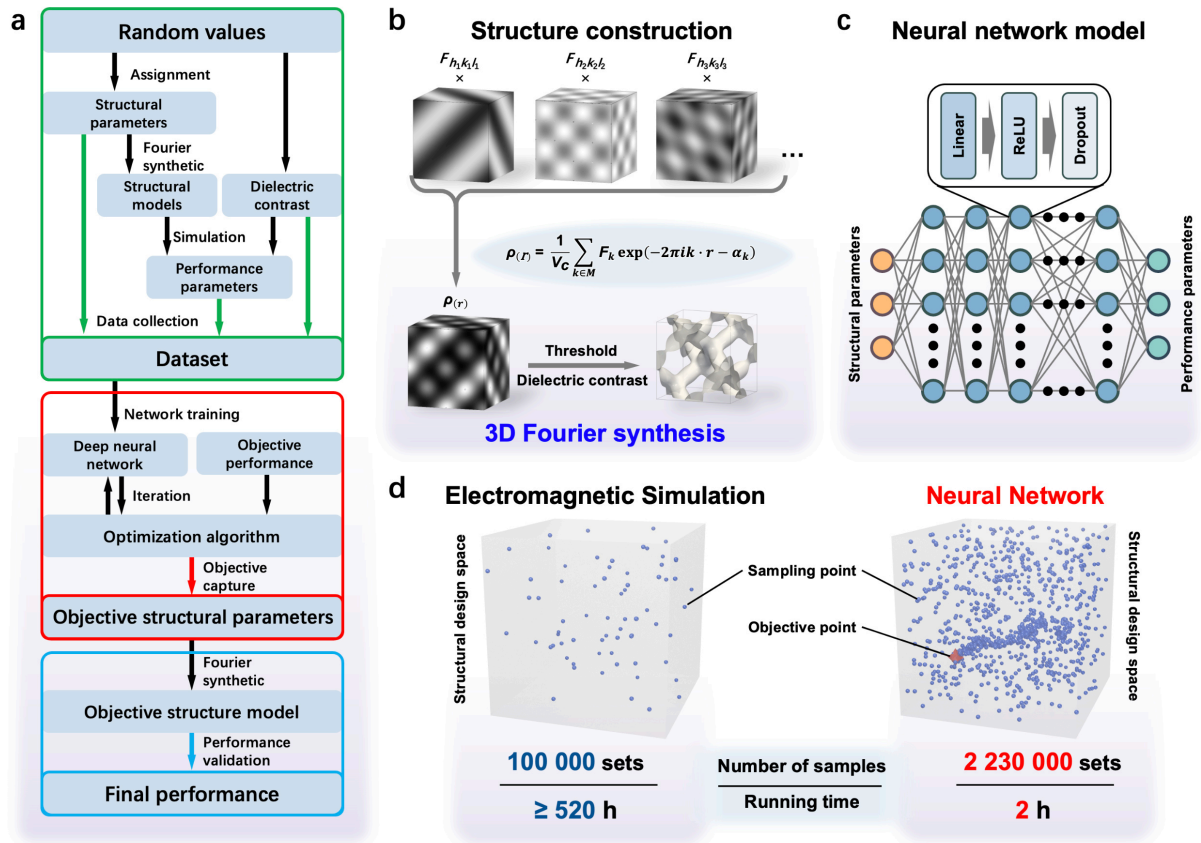


Fig. 1 Schematic workflow of the construction model by Fourier synthesis and the structural design using a deep neural network. **a** Schematic diagram of the workflow. A random sampling of the structural design space was achieved by Fourier synthesis with random parameters in Eq. (1) combined with the dielectric contrast to calculate the performance parameters by electromagnetic simulation. The structural parameters, dielectric contrast and performance parameters were collected to construct a dataset (green box) to train the deep neural network. The deep neural network was combined with genetic optimization algorithm to capture the objective structural parameters (red box) through an iterative process with a predefined performance objective. The objective structure was constructed again by Fourier synthesis and its performance was verified by electromagnetic simulation (blue box). **b** The construction of photonic structures by Fourier synthesis. **c** The neural network model architecture using multilayer perceptron. The structural parameters and performance parameters (photonic band structure) were used as input and output data of the neural network, respectively. The Rectified Linear Unit (ReLU) function was used as a nonlinear activation and Dropout was added to prevent overfitting after each hidden layer. **d** Comparison of the efficiency of electromagnetic simulation versus neural network for the exploration of the structural design space. The sampling of 100 000 sets of samples by electromagnetic simulation for the structural design space took more than 520 h. The neural network took only 2 h to explore the structural design space for 2.23 million sets of samples during the structural design process. The efficiency of sampling the structural design space is, therefore, improved by more than three orders of magnitude.

2. Results and Discussion

2.1 Modeling of photonic structures by Fourier synthesis

Generally, the formation of a CPB is considered to be the result of coherent scattering of electromagnetic waves by the photonic crystal.^{3,4} The scattering process should, however, not be understood in the form of a Born series, which does generally not converge for practical refractive index contrasts. Instead, a classification with respect to the translation symmetry of the crystal using Bloch's theorem can explain the occurrence of a bandgap through an absence of available photonic states in the material.¹ A large CPB requires an absence of states in all directions of propagation, which can be addressed by structures with the most spherical Brillouin zone.⁴⁰ Additionally, connected low-coordination-number networks of uniform valency possessing substantial local self-uniformity are considered conducive to the formation of large CPBs.^{20,41} To date, the face-centered cubic single diamond (SD, *dia* net, space group $Fd\bar{3}m$, No. 227) structure with tetravalent vertices is considered the “holy grail” of all photonic structures due to the most isotropic and highly geometrical identical framework, exhibiting the widest photonic bandgap and the lowest dielectric contrast requirement.^{5,8,20} The body-centered cubic, chiral single gyroid (SG, *srs* net, space group $I4_132$, No. 214) structure with trivalent nodes, which also exhibits perfect local self-uniformity, also forms a large CPB comparable to but smaller than the diamond.^{10,41} It is worth noting that these two structures have also been found to be the source of structural colors in various biomineralized skeletons and scaffolds.^{42–46} In addition, the single primitive (SP, *pcu* net, space group $Pm\bar{3}m$, No. 221) network also produces a relatively smaller CPB in simulations,^{10,30} which can be attributed to the fact that it consists of hexavalent nodes with less local self-uniformity.⁴¹ Considering the excellent photonic properties of these structures, we apply our method to the corresponding space groups.

We also consider the space groups of their correlated double-network morphologies, namely, of the self-dual double diamond (DD, *dia-c* net, space group $Pn\bar{3}m$, No. 224), the achiral double gyroid (DG, *srs-c* net, space group $Ia\bar{3}d$, No. 230) and self-dual double primitive (DP, *pcu-c* net, space group $Im\bar{3}m$, No. 229) network. The multi-network structures are capable of demonstrating fascinating phenomena, such as 3D Weyl points and large circular polarization stop bands.^{16,47} However, it has been proposed that these double-network eliminate the bandgap properties.¹⁰ Even so, exploring the photonic structure within these symmetries remains appealing, as it holds the potential to transcend existing cognitive boundaries.

We, therefore, concentrate our explorations in this paper using these six space group symmetries. We build the structural models by Fourier synthesis using structure factors F_{hkl} applying the calculation rules in *International Tables for X-Ray Crystallography*.²⁵ Five representative low-index Bragg reflections (abbreviated as reflections) were chosen for effective conceptual validation of our workflow. Each unique hkl reflection corresponds to a group of $\{hkl\}$ Fourier coefficients, which possess identical amplitudes but their phases are related through symmetry operations. Prior to substitution into the calculation equations, each unique reflection was expanded to encompass all symmetry-related ones. The selection and reflections for the space groups and the calculation equations are listed in **Table S1-S7**. The crystal structures modeled with different structural parameters in each space group are illustrated in **Figure S1-S6**.

The crystal structure model can be tuned by adjusting the values of the structural parameters (**Figure 2**). **Animation S1** show the crystal structure models corresponding to different threshold t values in the space group $Fd\bar{3}m$ when only the 111 reflection is finite ($F_{111} = 1.0, F_{220} = 0.0, F_{311} = 0.0, F_{222} = 0.0, F_{400} = 0.0$). As t is the normalized threshold value in the range of $[0, 1)$ as defined in Eq. (2), the structural interface is similar to the diamond triply periodic minimal surface for $t = 0.5$. For $t = 0.3$ and 0.7 , the structure exhibits a SD structure

with complementary feature. By continued increase of t to 0.9, it transforms into simple structural units (rounded tetrahedra) orderly distributed at diamond lattice coordinate points. As shown in **Animation S2-S5**, by adjusting the other coefficients separately based on the structural parameters of $F_{111} = 1.0$ and $t = 0.5$, we were able to generate rich structural models. This includes many complex surface structures that cannot be constructed from simple structural units (e.g., spheres, cylinders, etc.). These structural variations lead to corresponding

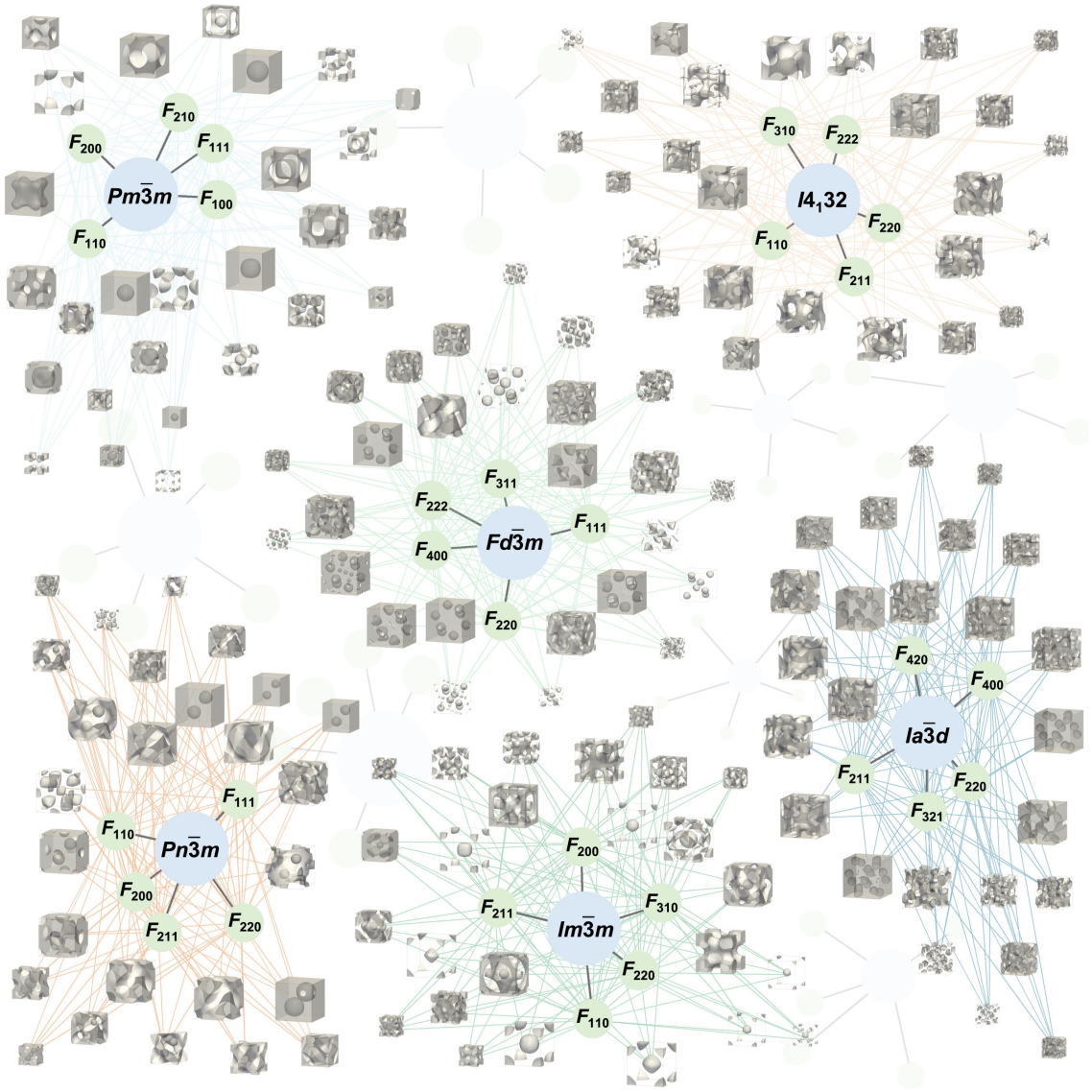


Fig. 2 Representative photonic crystal models obtained by different structural parameters associated with the corresponding space group symmetries.

changes in their photonic properties. The band structures of these structures calculated under a dielectric contrast of 13.00 are also shown in the animations. The structural diversity, design flexibility and complexity of the Fourier synthesis-based modeling approach are illustrated in **Figure 2**.

2.2 Exploration of photonic bandgap performance space

The structural parameter range was determined by comparing the proportion of structures with CPB (>1%) under different structural parameter settings. Taking the space group $Fd\bar{3}m$ (227) as an example, 1 000 candidate structures were generated by random structural parameters of five low-index reflections. Notably, for centrosymmetric structures, the structure factor phase can only be 0 or π , which is reflected in the calculation through the sign of the structure factor amplitude, where the positive numbers correspond to a phase of 0 and the negative value correspond to a phase of π . Since the space group $I4_132$ (214) exhibits a non-centrosymmetric structure, its phase combinations will result in an excessively large structural design space. Consequently, the phases were referenced to the SG structure and confined to 0, $\pi/2$, π , and $3\pi/2$, to guarantee a high probability of CPB structures (**Tables S2-S7**). The corresponding band structures (performance space) were calculated using MPB with the dielectric contrast of 13.00 for the filling material. As shown in **Table S8**, the probability of photonic structures varies with the data range of the five reflections. The highest probability occurred when the amplitude of the first reflection was set to 1 and the other four reflections were in the range of $[-1, 1)$, where ~15% of the 1 000 structures exhibited CPB. In this scheme, the first reflection provides the largest contribution to the structure, and other reflections would modulate the structure on this basis. Therefore, this setting was used in subsequent calculations to ensure computational efficiency.

Within the parameter range of the above-mentioned design space, 10 000 models were randomly sampled for each of the six space groups. The corresponding band structures were calculated by MPB. CPB structures were found in all space groups (**Figure 3** and **Table S9**).

Particularly, the space group $Fd\bar{3}m$ possessed over 1 700 CPB structures and showed a

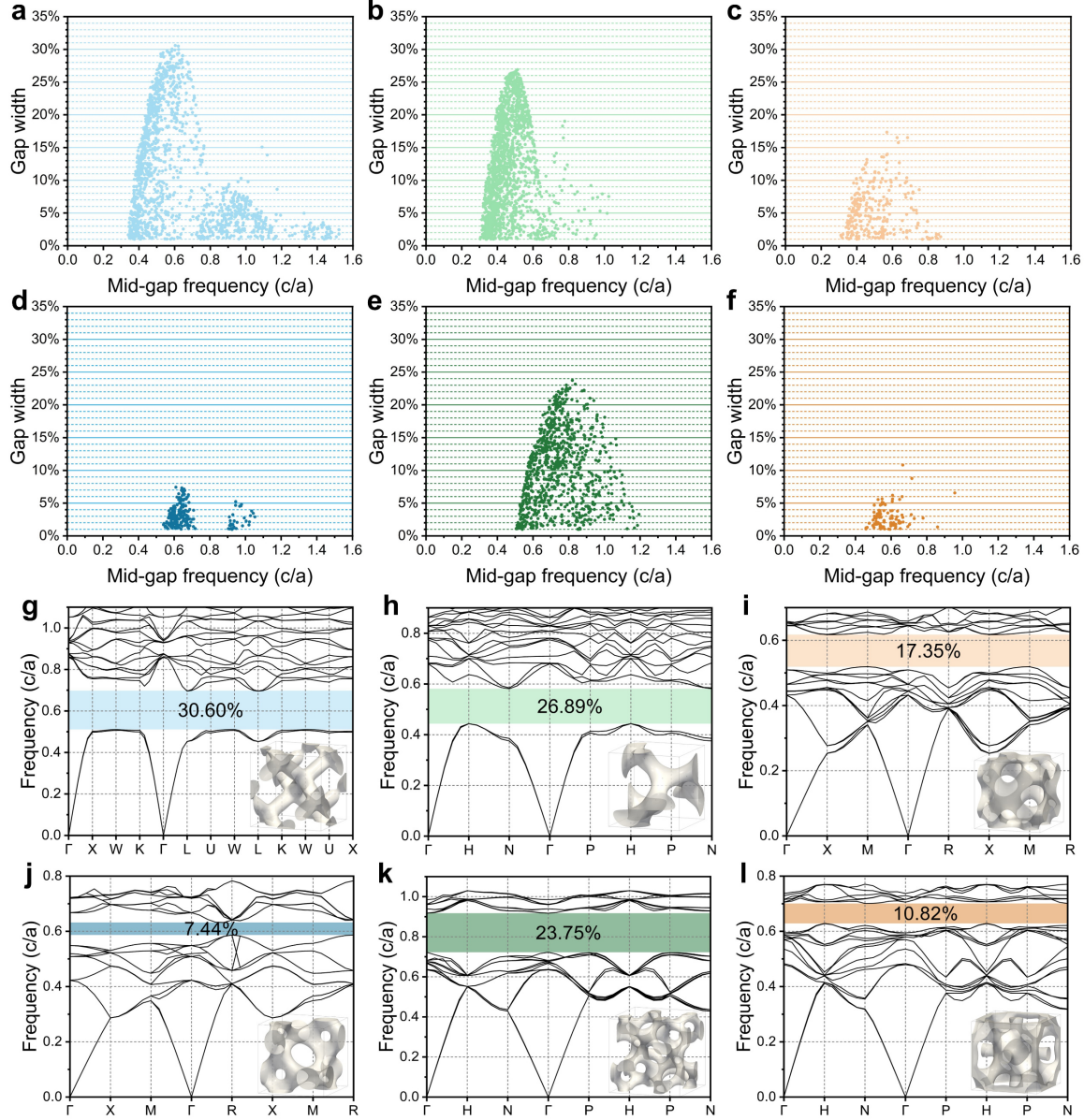


Fig. 3 Photonic bandgap properties of different space groups. **a-f** Performance space for each space group of (a) $Fd\bar{3}m$, (b) $I4_132$, (c) $Pm\bar{3}m$, (d) $Pn\bar{3}m$, (e) $Ia\bar{3}d$, (f) $Im\bar{3}m$ with dielectric contrast of 13.00. **g-l** Structures with the largest gap width found in each space group and their band structures, (g) $Fd\bar{3}m$, (h) $I4_132$, (i) $Pm\bar{3}m$, (j) $Pn\bar{3}m$, (k) $Ia\bar{3}d$, (l) $Im\bar{3}m$. The k -path refers to Stefano Curtarolo's suggestion.⁴⁸

maximum gap between frequencies (f) 0.5111-0.6958 c/a with a gap width of 30.60%. The $I4_132$ structures also showed excellent photonic properties with the widest gap width of 26.89% between f range 0.4436-0.5814 c/a . The CPB structures also existed in other space groups, in particular, nearly 1 000 CPB structures were identified in space group $Ia\bar{3}d$. Although the widest gap width (23.75%) was lower than that of the $Fd\bar{3}m$, the f range 0.7228-0.9176 c/a was even higher than that of $Fd\bar{3}m$. Its CPB occurs at a very high band index between band 12 and 13. In fact, the connectivity index based on crystal symmetry alone, only allows a bandgap to open above the 8th band in $Ia\bar{3}d$.⁴⁹ Additionally, the $Ia\bar{3}d$ structure is geometrically more complex, with a genus of 13 per primitive unit cell, compared to a genus of 3 for the gyroid and the diamond. The relevant scattering dimension for destructive interference is therefore smaller compared to the unit cell, further explaining the occurrence of the bandgap at higher frequencies. For the other three space groups, the number of structures capable of forming CPBs was less than 3% of the total structures, and the gap width obtained was below 18%. In comparison, the space group of the more common inverse opal 3D photonic structure (space group $Fm\bar{3}m$, No. 225) hosted 4.05% CPB structures in all models with a lower maximum gap width of 15.84% (Figure S7).

2.3 Exploration of bandgap properties and design of structures with $Fd\bar{3}m$ symmetry

Considering the excellent photonic properties of the $Fd\bar{3}m$ symmetry, we further incorporated the dielectric contrast from 1.00 to 16.00 into the structural design parameters. 100 000 models with different parameter combinations were constructed, and the corresponding photonic properties were calculated. As shown in Figure S8, a minimum dielectric contrast of 3.87 was required to open a CPB, and the gap width increased with increasing the dielectric contrast. Among the 100 000 models, 8 392 samples yielded a CPB greater than 1%, with the mid-gap frequency (f_{mg}) in the range of 0.3091-1.2433 c/a (Figure 4a). In particular, the structure

possessing the widest bandgap (with detailed structural parameters presented in **Figure S9**) exhibits a 34.55% CPB in the f range of 0.4735-0.6713 c/a accompanied by a dielectric contrast of 15.35 and a gap width of 30.88% in the f range of 0.5089-0.6948 c/a with a dielectric contrast of 13.00. We further confirmed the bandgap of this structure using a high resolution of $32 \times 32 \times 32$ and obtained consistent results (34.99% and 31.31%, respectively). It is worth noting that, both the structure with the largest gap width and the CPB structure with minimum dielectric contrast are related to the SD structure with *dia* topology, albeit with different structural parameters. Judging from the results of the 100 000 samples, the performance parameters shown in **Figure 4a** should be close to the upper limit of optimized performance.

A fully connected multilayer perceptron (MLP)^{31,34} was trained using the dataset consisting of 100 000 samples described above to enable direct prediction of the corresponding band structures from the structural design parameters. The tested MLP hyperparameters with the corresponding losses and the loss for the validation dataset of the optimal MLP model are shown in **Figure S10** and **S11**. The MLP successfully predicted 794 out of the 882 structures with CPB in the test dataset. An example of the predicted band structure is shown in **Figure 4b** (structural parameters are listed in **Table S10**), which is highly consistent with the electromagnetic simulation. Moreover, the predicted f_{mg} and gap width concentrated around the ideal electromagnetic simulation results (**Figure 4c** and **Figure S12**), further illustrating the high accuracy of the bandgap performance obtained by the MLP.

The trained MLP combined with the genetic algorithm is capable of searching and iteratively optimizing the geometric structural design parameters with the target bandgap performance. For inverse structural design, the f_{mg} (0.6 c/a) and the gap width (20%) were chosen as two optimization objectives as an example. The dielectric contrast 13.00 of the material was used as a constraint. The structural design parameters (the structure factors shown in **Table S1** and the threshold t) were iteratively optimized (**Figure S13**). 2.23 million sets of structural parameters were evaluated within 2 h using a desktop workstation containing two

3.2-GHz Intel(R) Xeon(R) 6146 CPUs and an NVIDIA Quadro P2000 GPU. The band structures of the resulting geometries were computed with MPB to verify the performance of the optimized geometries. **Figure S14** shows the photonic bandgap performance for 18 sets of parameters obtained from the geometrical design space. As shown in **Figure 4d**, **S15** and **S16**, the results predicted by the MLP were close to those calculated by the electromagnetic simulation, and their performances met the original design requirements well. Interestingly, the resulting structures were diverse, including not only network structures but also hybrid structures with disconnected geometrical domains coexisting with percolating networks.

2.4 Exploration of bandgap properties and design of structures with $I4_132$ symmetry

As shown in **Figure 3b**, the space group $I4_132$ also showed diverse possibilities of well performing photonic structures. 8 616 samples with CPB greater than 1% were found among 100 000 sets of structural parameters calculated by electromagnetic simulation. As shown in **Figure 4e** and **S17**, the minimum dielectric contrast of 4.89 was identified in space group $I4_132$ for a CPB to appear, significantly larger than the value of 3.87 found for the space group $Fd\bar{3}m$. The widest gap of 31.87% in space group $I4_132$ was generated from a structure characterized by 110 and 211 reflections with similar amplitude but opposite phase (specific structural parameters are shown in **Figure S18**) at a dielectric contrast of 15.85 with the f range between 0.4027 and 0.5554 c/a , pointing to a SG-like structure with *srs* topology. The gap width of the structure was 26.78% in the f range 0.4400-0.5760 c/a for dielectric contrast of 13.00. These results were also consistent with the resolution of $32\times32\times32$ (31.64% and 26.83%, respectively).

Using the same workflow as for $Fd\bar{3}m$, a fully connected MLP was trained to map the structural parameters to the band structure. The validation dataset loss of the model training process is shown in **Figure S19**. The photonic band structures predicted by the MLP were in high agreement with the electromagnetic simulations (**Figure 4f** and the structural parameters

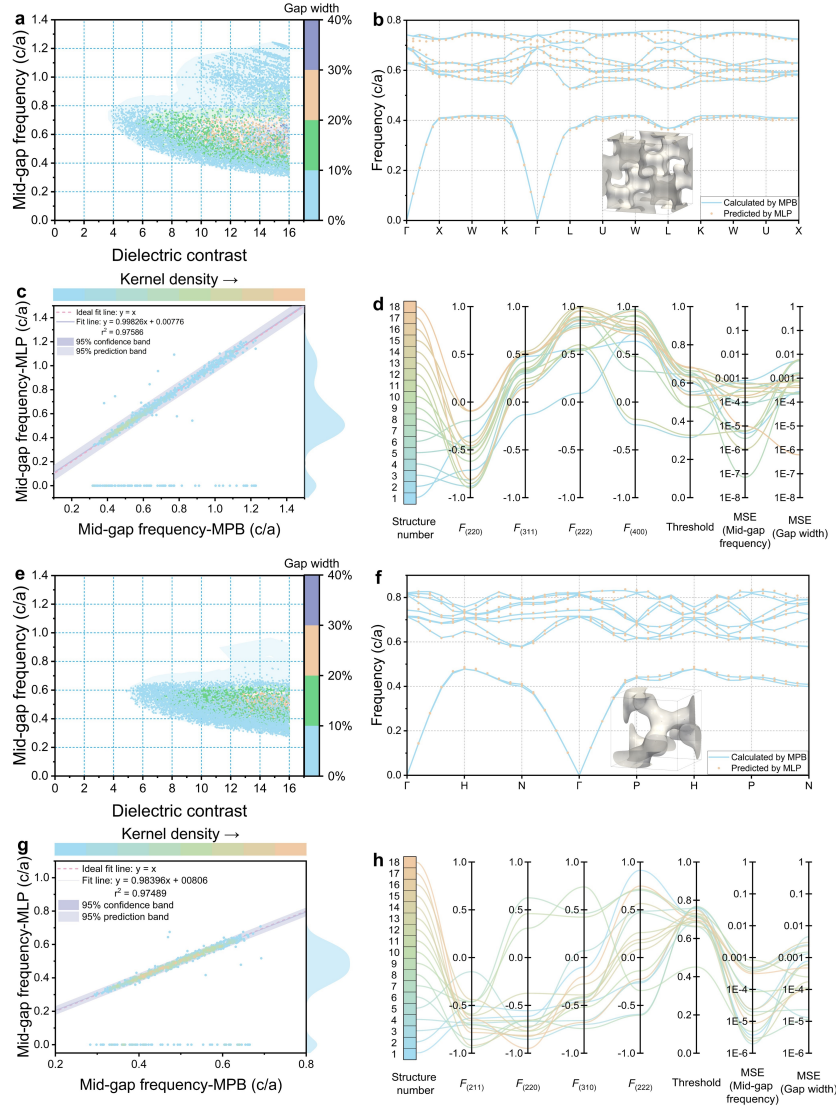


Fig. 4 Prediction and inverse design of photonic crystal performance based on MLP of $Fd\bar{3}m$ and $I4_132$ symmetries. **a** Design space of photonic bandgap performance parameters in the dataset of $Fd\bar{3}m$. **b** Photonic band structure of one representative sample in the test dataset calculated by MPB (blue line) and predicted by MLP (orange dots) in the space group $Fd\bar{3}m$ with a dielectric contrast of 15.98. The inset shows the structural model. **c** Correlation between the f_{mg} calculated by MPB and the predicted f_{mg} by MLP in the test dataset of $Fd\bar{3}m$. In this case, $f_{md} = 0$ means that there is no gap in the band structure. Samples that both have bandgap are used to compute the fit line. **d** Structural parameters of the photonic crystals with $Fd\bar{3}m$ symmetry obtained by MLP inverse design and the corresponding photonic bandgap performance with the mean-square error (MSE) of the target performance. **e** Design space of photonic bandgap performance parameters in the dataset of $I4_132$. **f** Photonic band structure of a representative structure calculated by MPB (blue line) and predicted by MLP (orange dots) in the space group $I4_132$ with a dielectric contrast of 10.11. The structural model is shown as inset. **g** Correlation between the MPB calculated f_{mg} and the MLP predicted f_{mg} in the test dataset of $I4_132$. **h** Structural parameters of $I4_132$ obtained by MLP inverse design and the corresponding bandgap with the MSE of the target performance.

are shown in **Table S11**). For the 877 sets of samples with CPBs in the test dataset, 780 of them were similarly predicted. As shown in **Figure 4g** and **Figure S20**, the predicted f_{mg} and gap width mainly concentrated around the electromagnetic simulation results. Based on the trained MLP, the inverse design of photonic crystal structures can, therefore, be applied. Taking the f_{mg} (0.5 c/a), gap width (15%), and dielectric contrast 13 as targets, the 18 sets of samples obtained through optimization well satisfied the original design requirements (**Figure 4h**, **S21-S23**).

2.5 Photonic structures with space group $Ia\bar{3}d$ as rivals of "holy grail" photonic crystal

Notably, the crystal structures with space group $Ia\bar{3}d$ also showed excellent photonic properties with high f_{mg} (**Figure 3e**). Therefore, 100 000 sets of random structural parameters and photonic bandgap performance parameters were generated by electromagnetic simulation. Among them, 6 232 sets of samples showed CPB greater than 1% with the f_{mg} between 0.4642-1.2357 c/a (**Figure 5a**). Particularly, the f_{mg} of the samples with gap widths greater than 20% ranged from 0.6106 to 0.9782 c/a . It is worth noting that a minimum dielectric contrast of 3.94 was required to ensure a CPB for $Ia\bar{3}d$ structure (**Figure 5b**, **S24** and **S25**), which is very close to the value of the $Fd\bar{3}m$ -based structures of 3.87. This structure consists of a connected network with nodes at (0.000, 0.250, 0.375) with $Ia\bar{3}d$ space group symmetry and the topology of an *lcs* network (**Figure 5c**). It can be described as an infinite tiling of space along four $\langle 111 \rangle$ directions by tiles composed of five hexagonal faces (**Figure 5d**).⁵⁰ Compared to the structures with $I4_132$ symmetry, this space group possesses much higher symmetry, the structure is achiral with complex connectivity and smooth saddle-shape surface. Notably, the structure with the maximum gap width was discovered with 321 and 400 reflections having a large amplitude with the opposite phase to the fundamental 211 reflection (the structural parameters are shown in **Table S12**). Under a computation resolution of $32 \times 32 \times 32$ in MPB, this structure creates a gap width of 24.75% between f range 0.7409-0.9501 c/a with a dielectric contrast of 14.31 and

a gap width of 23.04% in the f range 0.7722-0.9732 c/a with a dielectric contrast of 13.00. Using the same dielectric contrast of 15.35 as for the $Fd\bar{3}m$ structure, the gap width increased to 25.78% in the range of 0.7195-0.9325 c/a (**Figure 5e**). Due to the relatively high complexity of this structure, the results calculated at higher resolution are more accurate. For comparison, the gap widths are 25.91%, 24.17% and 27.72% for dielectric contrasts of 14.31, 13.00 and 15.35, respectively, calculated with a mesh size of $16 \times 16 \times 16$. Although the gap width is still smaller than that of $Fd\bar{3}m$, the gap frequency range is improved by 7.2% (**Figure 5f**). Additionally, the concurrent increase in f_{mg} resulted in a larger length scale required to control the same frequency range of light waves, which is beneficial for reducing the demand for manufacturing precision.

There is an ostensible increase in f_{mg} compared to the diamond-like morphology in the lcs structure, which suggests that it reduced the requirements for manufacturing precision in top-down fabrication. However, the lcs topology is structurally more complex within the unit cell, with vertices on the 24d Wyckhoff positions (compared to only 8a in the case of the diamond), and 48g mid-edge positions (compared to 16c), resulting in a genus of 13 (number of rings) per primitive unit cell (compared to a genus of only 3 for the diamond). The lcs and the dia net are both 4-coordinated and lead to tiling with 6-ringed facets. They only differ in the number of facets per tile (5 in case of the lcs and 4 in case of the self-dual dia), and the bond angles (100 and 132 degrees for the lcs and 110 degrees for the dia). Given the similarities of these two nets, the structural complexity is best covered by a frequency that is measured in units of c/d instead of c/a , where d is the edge length of the network. In these units, the f_{mg} of the lcs bandgap at refractive dielectric contrast 13.00 is 0.2672, and that for the dia is 0.2591. Even though the advantage in fabrication complexity is small, the bandgap opens at a similar refractive dielectric contrast for the dia and the lcs net, warranting further investigation of the latter. Meanwhile, it seems at least possible that more complex 3 or 4-coordinated geometries can rival or even beat the diamond as the reigning photonic bandgap champion structure.

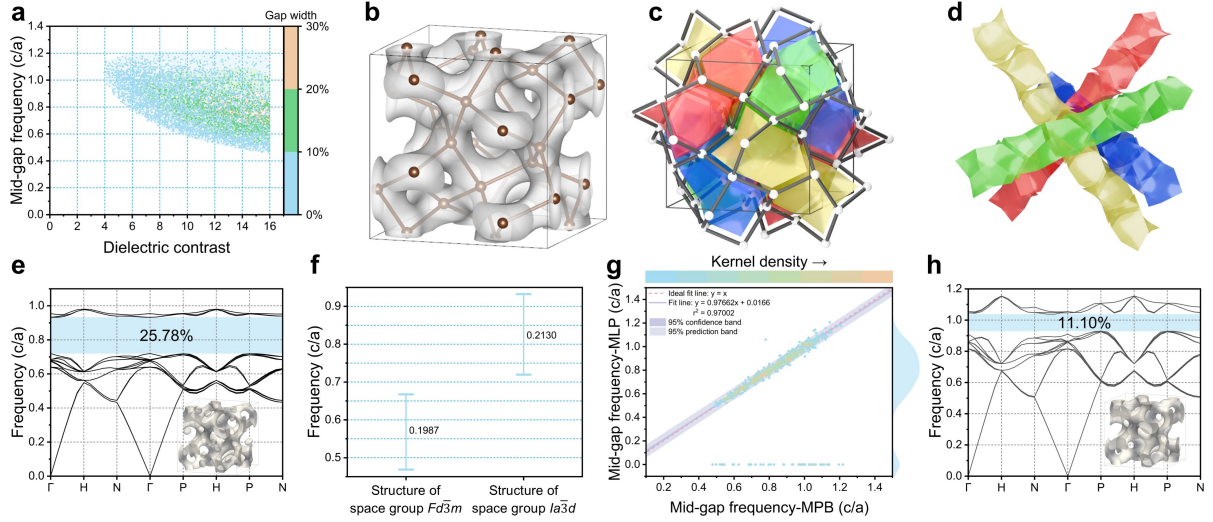


Fig. 5 Prediction and inverse design of photonic crystal performance based on MLP of $Ia\bar{3}d$ symmetry. **a** Design space of photonic bandgap performance parameters in the dataset. **b** CPB photonic structure with the minimum requirement of dielectric contrast (3.94) of $Ia\bar{3}d$. **c** Tessellation model of the structure in **b**. **d** Fragments of the lcs tiling. **e** The photonic band structure with the maximum gap width in the dataset (dielectric contrast of 15.35) and the corresponding geometry. **f** Photonic gap frequency range of the structures in $Fd\bar{3}m$ (Figure S9a) and $Ia\bar{3}d$ (**e**), both with dielectric contrast of 15.35. **g** Correlation between the mid-gap frequency calculated by MPB and those predicted by MLP in the test dataset. **h** Photonic band structure and geometrical structure with maximum gap width obtained by inverse design with dielectric contrast of 6.25.

The MLP was trained based on the 100 000 sets of geometrical structural parameters and photonic bandgap data. The validation dataset loss of the model training process is shown in Figure S26. As shown in Figure 5g and Figure S27, 651 sets of samples of interest showed CPB in the test dataset, and the f_{mg} of 597 sets of predicted structures were highly consistent with the electromagnetic simulation results, demonstrating the accuracy of the MLP. Then, the genetic algorithm was combined with the MLP to search for the structures with $Ia\bar{3}d$ symmetry with a wide photonic gap width. For the titania material with dielectric contrast of 6.25, a maximum photonic gap width of 11.10% at a f range of 0.9288-1.0380 c/a was obtained. The performance was also calculated by MPB with spatial resolution of $32 \times 32 \times 32$ and the structural parameters are shown in Table S13, which also pointed to the similar network with lcs topology (Figure 5h). Figure S28-S30 show the inverse design of photonic crystal structures to achieve

the required f_{mg} ($0.8\ c/a$), gap width (15%) and material dielectric contrast 13.00. Based on our workflow, it is highly convenient to set various performance targets based on the band structure data predicted by the MLP to optimize the structural parameters of photonic crystals.

2.6 Discussion and Outlook

The close correlation between photonic crystal performance and structure places high demands on structural modeling to achieve maximum design flexibility with as few structural parameters as possible.⁵¹ This is difficult to achieve with traditional modeling methods.⁵² The Fourier synthesis, by freely adjusting the number of structure factors, can cater to the diverse structural design needs and effortlessly achieve a balance between the two requirements. Herein, the effective tuning of the structures was achieved using only 5 low-index reflections with a certain data range, while adding more high-index reflections and expanding the data range can improve structural resolution and structural modulation in more detail in future research. Moreover, all 230 space group geometries can be introduced to the Fourier synthesis and arbitrary structures can be easily established and applied to our workflow by combining different Fourier components. Our method lends itself towards generating disordered photonic crystals within a computational supercell. In such a situation, the Fourier coefficients would be restricted to a thin spherical shell of radius much greater than the reciprocal lattice constant of the supercell^{41,53,54} with otherwise unconstrained hkl , corresponding to the absence of point symmetries. Since band structure calculations are very expensive in this scenario, MLP-assisted design might prove a vital ingredient in identifying and understanding disordered photonic crystals with large isotropic bandgaps.

The freely controllable number of structural parameters in Fourier design makes it convenient to combine it with the most fundamental fully connected MLP and achieve satisfactory prediction accuracy and structural design requirements without the involvement of complex neural networks in structural data processing. The deep learning method is able to

predict results at high speed with satisfactory accuracy requirements, which is different from the accurate description of physical phenomena by traditional electromagnetic simulation.^{31,32,34,51,55–57} By serving as a proxy mode for mathematical models describing physical phenomena, the efficiency in photonic structural design is thus greatly improved, opening pathways to the design of functional materials beyond bandgap optimization. This includes topological photonic crystals,⁵⁸ where a certain symmetry can predict band degeneracies with unique physical properties, but optimization is needed to achieve frequency isolation of these degeneracies,⁵⁹ and nonlinear photonic crystals,⁶⁰ for which phase matching is crucial. More generally, 3D metamaterial design⁶¹ would greatly benefit from a slightly modified approach, replacing MPB with an eigensolver that can model the associated physical system.

Although it is theoretically possible to generate CPBs in any space group,⁷ various general guidance rules to obtain larger bandgaps have been proposed for structural design, e.g., for low-genus simple structures, where the strut length is on the order of the lattice constant, face-centered cubic lattices with most spherical Brillouin zones would be favorable for the alignment of band gaps in all propagation directions to form a CPB.^{5,8,10,62} Besides, bicontinuous interwoven domains of high and low refractive index allow the electric field to concentrate best in the high index region, thereby maximizing the frequency difference between valence and conduction band.¹ For this reason, the single network topologies exhibit superior bandgap performance, while the corresponding double networks do not exhibit a CPB.¹⁰ The excellent bandgap properties of SD-based structures⁸ have been confirmed in our work. The SD structure (*dia* net) with space group $Fd\bar{3}m$ produced CPBs with a minimum requirement of dielectric contrast and yielded the largest gap width. Similarly, the SG-based structure (*srs* net) with symmetry $I4_132$ also showed excellent photonic bandgap properties. Notably, the $I4_132$ *srs* structure is intrinsically chiral and features chiral-optical properties.⁶³ This aspect was not

addressed in this article, but strong circular dichroism or optical rotation found in multi-*srs* topologies^{47,64} could be improved with our approach.

However, our study already revealed that the 3D photonic structure with *lcs* topology with space group $Ia\bar{3}d$ deserves more attention. $Ia\bar{3}d$ is the space group of the DG structure (*srs-c* net) with a body-centered cubic lattice and consists of tetravalent nodes and hexagonal shortest rings such as the SD (*dia* net), however, with different arrangement.⁶⁵ Remarkably, the *lcs* net is the skeletal graph of the so-called G' structure, a member of the $C(I_2-Y^{**})$ family discovered by von Schnering and Nesper.^{27,65,66} Although the photonic crystal properties of the $C(I_2-Y^{**})$ structure have been realized two decades ago,³⁰ this structure does not seem to have attracted much attention, and its network topology has not been revealed.

To further compare the photonic bandgap characteristics of the structures under these three space groups, the structures were further optimized under the constraints of dielectric contrasts of 6.25 and 13.00, respectively. As shown in **Table 1**, the gap width and gap frequency range of the *lcs* net are better than those of *srs*-based structures and even comparable with the *dia* net. It is worthy to note that, Bragg scattering comes from perfectly periodic structures, but interference can also occur between scattering centers in the absence of crystallographic symmetry.⁵⁴ Potential candidates for CPB materials should be composed of geometrically identical scattering units because increasing the spatial similarity of the scattering units will maximize the overlap of their spectral ranges that suppress propagation, thus facilitating the formation of CPBs. In 3D space, tetravalent and trivalent networks, both have low coordination numbers and maximum local self-uniformity, have been demonstrated to be capable of generating large CPBs.⁴¹ From the structural point of view, the *lcs* topology contains all the factors needed to design an ideal photonic crystal. The lattice shows strong isotropy of the tetravalent scattering units with good, albeit not perfect, local self-uniformity. The exceptional bandgap performance of the *lcs* topology, particularly its minimum requirement for dielectric contrast with open CPBs comparable to SD structures (*dia* net) and its large gap frequency

Table 1. Bandgap properties of photonic crystal structures with the largest photonic gap width in the structures with *dia*, *srs* and *lcs* topology optimized under dielectric contrast of 6.25 and 13.00, respectively.

The corresponding geometries and band structures are shown in **Figure 5h**, **S31** and **S32**, and were calculated by the MPB with the spatial resolution of 32×32×32.

Topology	Dielectric contrast	$f_{\text{mg}} (c/a)$	Gap width	Gap f range (c/a)
<i>dia</i>	6.25	0.6602	13.86%	0.0915
	13.00	0.6041	31.24%	0.1887
<i>srs</i>	6.25	0.5651	8.07%	0.0456
	13.00	0.4867	27.47%	0.1337
<i>lcs</i>	6.25	0.9834	11.10%	0.1092
	13.00	0.8283	24.37%	0.2019

range at higher mid-gap frequencies, confers its unique advantages in the fabrication of optically controlled devices.

In our calculations, there are also a large number of hybrid structures with disconnected nodes coexisting with network structures showing large CPBs (**Figure S15**, **S22** and **S29**). Based on the inspiration brought by the effect of connectivity on the band gap in 2D structures,^{22,67} a variety of 3D photonic crystal-based methods have also demonstrated that not only network structures^{19,20} but also disconnected geometries^{6,7} are capable of forming CPBs. The hybrid structures that emerge in our work provide an extra complement to photonic structural design. At the same time, three-component structures are often experimentally obtained through backfilling a mold with high-index materials⁶⁸ but are rarely studied. The Fourier synthesis is ideally suited to study such multi-component materials by introducing an additional threshold in Eq. (1). Even more so, the Fourier sum describes a thresholdless continuous variation of permittivity that is computationally favourable as it allows the plane wave expansion in MPB to converge exponentially⁶⁹ and might lead to unprecedented large PBGs as it widens the parameter space. Moreover, our results demonstrate that large bandgaps

are also robust to discrete substructure units in network structures. This complements the previous view that large bandgaps are inherently robust to the roughness of structural surfaces.^{20,70} The above points indicate that our method for exploring photonic band structures reveals a rich diversity in photonic crystal architectures. Therefore, a single structural design rule does not apply to all photonic structures, and existing structural design methods may have inherent limitations.

Our workflow not only provides guidance for the design of photonic structures, but may also point out new possibilities for its fabrication and reduce the difficulty of fabrication. Currently, the fabrication of photonic crystals primarily encompasses bottom-up self-assembly techniques and top-down physical approaches. The single-networks such as the SD and SG structures have been successfully constructed by a template-filled or kinetically-controlled block copolymer self-assembly method with inorganic participation.^{68,71–78} Moreover, in the theoretical self-assembly phase diagrams of asymmetric miktoarm star copolymers, a series of sphere-network hybrid structures were obtained.^{79,80} These structures are very similar to the hybrid structures we found, which may also be synthesized by block copolymer microphase separation. Besides, with the development of additive manufacturing and other fabrication techniques, the arbitrary design employed in this research can be transcribed into practical materials. For instance, the two-photon polymerization technology has been employed to fabricate 3D structures with sub-micrometer precision.^{81–83} As manufacturing technologies continue to evolve, it will also become feasible to directly produce 3D photonic crystals with desired optical properties.⁸⁴

3. Conclusion

In summary, we demonstrated the power of Fourier synthesis free modeling of photonic crystals and introduced a novel paradigm that empowers the exploration and design of photonic crystal structures that meet specific bandgap performance requirements. The robust and flexible

workflow transcended the limitations of traditional experience-based design approaches for photonic crystal structures. Based on our workflow, the excellent photonic bandgap properties of SD- and SG-based structures were demonstrated and the inverse design of the structures was achieved. Furthermore, searching in space group $Ia\bar{3}d$ revealed the *lcs* topology can rival the properties of the traditional "holy grail" SD photonic crystals. We anticipate that within the broader structural design space, there are many more photonic structures with exceptional performance waiting to be uncovered. The approach of this work can pave the way for obtaining rich and fascinating optical applications.

4. Experimental Section

Structural modeling by Fourier synthesis

The photonic structures were modeled by Fourier synthesis using structure factors F_{hkl} of selected hkl reflections with reference to the calculation formulas in *International Tables for X-Ray Crystallography* (Table S1-S7).²⁵ Taking space group $Fd\bar{3}m$ as an example, structure factor amplitudes of 111, 220, 311, 222, 400 reflections and the isosurface threshold t with random values were used as structural parameters. Before inputting the equation, each unique reflection was expanded to all equivalent reflections and the crystal factor phases were changed according to crystal symmetry. Then the $\rho(r)$ for all coordinates (r) in space were computed to form the level set. After normalization based on the minimum and maximum values of the electron density, the space with normalized electron density $\rho_{norm}(r)$ can be divided into two regions using a threshold t . In this study, it was defined that the material with dielectric contrast greater than 1 was occupying the space where $\rho_{norm}(r) > t$, and vice versa. Different geometries were obtained by changing space group symmetries and adjusting the geometric structural parameters.

Photonic band structure calculation and dataset construction

The computation of the photonic band structure was performed using MIT Photonic-Bands (MPB) based on plane wave eigenmode search.³⁹ The k -paths in reciprocal space referred to the suggestions provided by Stefano Curtarolo.⁴⁸ And the resolution was set to 16. For the construction of the dataset, the first structure factor amplitude in the geometrical structural parameters was specified as 1, and the remaining structure factor amplitudes were assigned in the range of -1 to 1 with random values. The threshold t was randomly generated between 0 and 1, and the dielectric contrast was randomly assigned between 1 and 16. The geometrical structural parameters and dielectric contrast were inputted into the MPB and the corresponding photonic band structures as well as gap properties were calculated. The results of all calculations were summarized into the dataset.

Neural network architecture and training

The dataset consisting of 100 000 samples was randomly divided into a training dataset (70%), a validation dataset (20%) and a test dataset (10%). The open source PyTorch was employed to construct multilayer perceptron (MLP) with multiple hidden layers. The neural network model contained six neurons in the input layer, each corresponding to the amplitudes of the structure factor for the last four selected reflections, the threshold t and the dielectric contrast of the material. All input parameters were normalized to $[0, 1]$ in their respective value ranges before feeding them to the neural network. The discrete data points of the photonic band structure data were transformed into a one-dimensional array, which then corresponded one-to-one with the neurons in the output layer of the neural network. Rectified Linear Units (ReLUs) were added as activation functions. Dropout was added after each hidden layer to prevent overfitting for neural network training. The loss was evaluated using the mean-square error (MSE) loss function

$$MSE = \frac{1}{n} \sum_{i=1}^n (y_i - \hat{y}_i)^2$$

where n is the number of samples and \hat{y}_i and y_i are the predicted and true values for sample numbered i . Adam optimizer was used for training the neural network. The trained MLP was able to directly predict the corresponding photonic band structure data from the structural parameters, and the corresponding gap performance can be obtained through a simple post-processing step.

The hyperparameters (batch size, number of hidden layers, number of neurons in each hidden layer, learning rate, dropout size and number of epochs) were optimized using the Bayes method that comes with the wandb library. The optimized MLP contained 7 hidden layers and 2 048 neurons per hidden layer. 5 000 samples were fed to the neural network per batch during training. The learning rate of the Adam optimizer and the dropout size were set to 0.00001 and 0.1. After 3 000 epochs, the loss of MLP almost stopped decreasing.

Inverse design of photonic crystal structures

The Non-dominated Sorting Genetic Algorithm II (NSGA-II)³⁷ provided by the open source multi-objective optimization algorithm library pymoo⁸⁵ was used in combination with the trained MLP for inverse design of photonic crystal structures with predefined properties. The general approach was to search the structural design space of the photonic crystal, namely the amplitudes of the four structural factors mentioned above and the threshold t , using the predefined mid-gap frequency and gap width as the optimization objectives and the specified material dielectric contrast as the constraint. Iterations were performed to minimize the MSE between the gap performance predicted by MLP and the predefined optimization objective. The inverted generational distance (IGD) was employed as a metric to simultaneously evaluate the convergence and diversity of the optimization process. The inverse structural design processes were performed on two 3.2-GHz Intel(R) Xeon(R) 6146 CPUs and an NVIDIA Quadro P2000

GPU for 120 min. The obtained structural parameters were used to construct the structure by Fourier synthesis and the final band structure was calculated using MPB at a spatial resolution of $16 \times 16 \times 16$ for initial search or $32 \times 32 \times 32$ for specific structures.

Acknowledgements

The authors thank Dr. Yuanyuan Cao, East China University of Science and Technology, for insightful suggestions and support in the completion of this article. This work was financially supported by the National Natural Science Foundation of China (Grant No. 22425303) and the Fundamental Research Funds for the Central Universities.

Author contributions

C.C. and L.H. designed the research. C.C. carried out experiments. C.C., M.S., L.H. wrote the manuscript. All authors critically revised the manuscript. L.H. guided all aspects of the work. All authors have given approval to the final version of the manuscript.

Data availability

The data that support the findings of this study are available from the corresponding author upon reasonable request.

Conflict of interest

The authors declare no competing interests.

Supplementary information

The online version contains supplementary material.

References

- 1 Joannopoulos, J. D., Winn, J. N. & Johnson, S. G. Photonic Crystals: Molding the Flow of Light - Second Edition. (Princeton University Press, 2011).
- 2 Joannopoulos, J. D., Villeneuve, P. R. & Fan, S. Photonic crystals: putting a new twist on light. *Nature* **386**, 143–149 (1997).
- 3 John, S. Strong localization of photons in certain disordered dielectric superlattices. *Phys. Rev. Lett.* **58**, 2486–2489 (1987).
- 4 Yablonovitch, E. Inhibited spontaneous emission in solid-state physics and electronics. *Phys. Rev. Lett.* **58**, 2059–2062 (1987).
- 5 Ho, K. M., Chan, C. T. & Soukoulis, C. M. Existence of a photonic gap in periodic dielectric structures. *Phys. Rev. Lett.* **65**, 3152–3155 (1990).
- 6 Maldovan, M., Ullal, C. K., Carter, W. C. & Thomas, E. L. Exploring for 3d photonic bandgap structures in the 11 f.c.c. space groups. *Nat. Mater.* **2**, 664–667 (2003).
- 7 Cersonsky, R. K., Antonaglia, J., Dice, B. D. & Glotzer, S. C. The diversity of three-dimensional photonic crystals. *Nat. Commun.* **12**, 2543–2549 (2021).
- 8 Maldovan, M. & Thomas, E. L. Diamond-structured photonic crystals. *Nat. Mater.* **3**, 593–600 (2004).
- 9 Ullal, C. K. et al. Triply periodic bicontinuous structures through interference lithography: a level-set approach. *J. Opt. Soc. Amer. A* **20**, 948–954 (2003).
- 10 Maldovan, M. et al. Photonic properties of bicontinuous cubic microphases. *Phys. Rev. B* **65**, 165123–165127 (2002).
- 11 Fan, S., Villeneuve, P. R. & Joannopoulos, J. D. Large omnidirectional band gaps in metallodielectric photonic crystals. *Phys. Rev. B* **54**, 11245–11251 (1996).
- 12 Yablonovitch, E. & Gmitter, T. J. Photonic band structure: the face-centered-cubic case. *Phys. Rev. Lett.* **63**, 1950–1953 (1989).

- 13 Saba, M. et al. Nature of topological protection in photonic spin and valley hall insulators. *Phys. Rev. B* **101**, 54307 (2020).
- 14 Maldovan, M., Carter, W. C. & Thomas, E. L. Three-dimensional dielectric network structures with large photonic band gaps. *Appl. Phys. Lett.* **83**, 5172–5174 (2003).
- 15 Doosje, M., Hoenders, B. J. & Knoester, J. Photonic bandgap optimization in inverted fcc photonic crystals. *J. Opt. Soc. Am. B* **17**, 600–606 (2000).
- 16 Lu, L., Fu, L., Joannopoulos, J. D. & Soljačić, M. Weyl points and line nodes in gyroid photonic crystals. *Nat. Photonics* **7**, 294–299 (2013).
- 17 Kim, S., Christensen, T., Johnson, S. G. & Soljačić, M. Automated discovery and optimization of 3d topological photonic crystals. *ACS Photonics* **10**, 861–874 (2023).
- 18 Li, W. et al. Topology optimization of photonic and phononic crystals and metamaterials: a review. *Adv. Theor. Simul.* **2**, 1900017 (2019).
- 19 Meng, F., Jia, B. & Huang, X. Topology-optimized 3d photonic structures with maximal omnidirectional bandgaps. *Adv. Theor. Simul.* **1**, 1800122–1800126 (2018).
- 20 Men, H. et al. Robust topology optimization of three-dimensional photonic-crystal band-gap structures. *Opt. Express* **22**, 22632–22648 (2014).
- 21 Liu, Z. et al. Generative model for the inverse design of metasurfaces. *Nano Lett.* **18**, 6570–6576 (2018).
- 22 Sigmund, O. & Hougaard, K. Geometric properties of optimal photonic crystals. *Phys. Rev. Lett.* **100**, 153904–153907 (2008).
- 23 Zimek, A., Schubert, E. & Kriegel, H. A survey on unsupervised outlier detection in high-dimensional numerical data. *Stat. Anal. Data Min.* **5**, 363–387 (2012).
- 24 Marimont, R. B. & Shapiro, M. B. Nearest neighbour searches and the curse of dimensionality. *IMA J. Appl. Math.* **24**, 59–70 (1979).
- 25 Henry, N. F. M. & Lonsdale, K. International Tables for X-Ray Crystallography. (The Kynoch Press, 1976).

- 26 Bruce, D. W., O'Hare, D. & Walton, R. I. *Structure from Diffraction Methods*. (Wiley, 2014).
- 27 Von Schnering, H. G. & Nesper, R. Nodal surfaces of fourier series: fundamental invariants of structured matter. *Z. Phys. B: Condens. Matter* **83**, 407–412 (1991).
- 28 Gandy, P. J. F., Bardhan, S., Mackay, A. L. & Klinowski, J. Nodal surface approximations to the p,g,d and i-wp triply periodic minimal surfaces. *Chem. Phys. Lett.* **336**, 187–195 (2001).
- 29 Mackay, A. L. Crystallographic surfaces. *Proc. R. Soc. Lond. A* **442**, 47–59 (1993).
- 30 Michielsen, K. & Koe, J. S. Photonic band gaps in materials with triply periodic surfaces and related tubular structures. *Phys. Rev. B* **68**, 115107 (2003).
- 31 Greener, J. G., Kandathil, S. M., Moffat, L. & Jones, D. T. A guide to machine learning for biologists. *Nat. Rev. Mol. Cell Biol.* **23**, 40–55 (2022).
- 32 Bender, A. et al. Evaluation guidelines for machine learning tools in the chemical sciences. *Nat. Rev. Chem.* **6**, 428–442 (2022).
- 33 Meuwly, M. Machine learning for chemical reactions. *Chem. Rev.* **121**, 10218–10239 (2021).
- 34 Ma, W. et al. Deep learning for the design of photonic structures. *Nat. Photonics* **15**, 77–90 (2021).
- 35 Artrith, N. et al. Best practices in machine learning for chemistry. *Nat. Chem.* **13**, 505–508 (2021).
- 36 LeCun, Y., Bengio, Y. & Hinton, G. Deep learning. *Nature* **521**, 436–444 (2015).
- 37 Deb, K., Pratap, A., Agarwal, S. & Meyarivan, T. A fast and elitist multiobjective genetic algorithm: nsga-ii. *IEEE Trans. Evol. Comput.* **6**, 182–197 (2002).
- 38 Aroyo, M. I. *International Tables for Crystallography: Space-Group Symmetry*. (International Union of Crystallography, 2016).

- 39 Johnson, S. G. & Joannopoulos, J. D. Block-iterative frequency-domain methods for maxwell's equations in a planewave basis. *Opt. Express* **8**, 173–190 (2001).
- 40 Yablonovitch, E. Photonic band-gap structures. *J. Opt. Soc. Am. B* **10**, 283–295 (1993).
- 41 Sellers, S. R., Man, W., Sahba, S. & Florescu, M. Local self-uniformity in photonic networks. *Nat. Commun.* **8**, 14439–14451 (2017).
- 42 Wilts, B. D. et al. Butterfly gyroid nanostructures as a time-frozen glimpse of intracellular membrane development. *Sci. Adv.* **3**, e1603119–e163127 (2017).
- 43 Galusha, J. W. et al. Discovery of a diamond-based photonic crystal structure in beetle scales. *Phys. Rev. E* **77**, 050904–050907 (2008).
- 44 Barrows, F. P. & Bartl, M. H. Photonic structures in biology: a possible blueprint for nanotechnology. *Nanomater. Nanotechnol.* **4**, 1–12 (2014).
- 45 Djeghdi, K., Steiner, U. & Wilts, B. D. 3D tomographic analysis of the order-disorder interplay in the pachyrhynchus congestus mirabilis weevil. *Adv. Sci.* **9**, 2202145 (2022).
- 46 Saranathan, V. et al. Evolution of single gyroid photonic crystals in bird feathers. *Proc. Natl. Acad. Sci. U.S.A.* **118**, e2101357118 (2021).
- 47 Saba, M. et al. Circular dichroism in biological photonic crystals and cubic chiral nets. *Phys. Rev. Lett.* **106**, 103902 (2011).
- 48 Setyawan, W. & Curtarolo, S. High-throughput electronic band structure calculations: challenges and tools. *Comput. Mater. Sci.* **49**, 299–312 (2010).
- 49 Christensen, T., Po, H. C., Joannopoulos, J. D. & Soljačić, M. Location and topology of the fundamental gap in photonic crystals. *Phys. Rev. X* **12**, 21066 (2022).
- 50 Delgado Friedrichs, O., O'Keeffe, M. & Yaghi, O. M. Three-periodic nets and tilings: regular and quasiregular nets. *Acta Crystallogr., Sect. A: Found. Crystallogr.* **59**, 22–27 (2003).
- 51 Liu, Z., Zhu, D., Raju, L. & Cai, W. Tackling photonic inverse design with machine learning. *Adv. Sci.* **8**, 2002923–2002937 (2021).

- 52 Park, J. et al. Free-form optimization of nanophotonic devices: from classical methods to deep learning. *Nanophotonics* **11**, 1809–1845 (2022).
- 53 Vogler-Neuling, V. V. et al. Biopolymer photonics: from nature to nanotechnology. *Adv. Funct. Mater.* **34**, 2306528 (2023).
- 54 Vynck, K. et al. Light in correlated disordered media. *Rev. Mod. Phys.* **95**, 45003 (2023).
- 55 Freire, P., Manuylovich, E., Prilepsky, J. E. & Turitsyn, S. K. Artificial neural networks for photonic applications—from algorithms to implementation: tutorial. *Adv. Opt. Photonics* **15**, 739–834 (2023).
- 56 Jiang, J., Chen, M. & Fan, J. A. Deep neural networks for the evaluation and design of photonic devices. *Nat. Rev. Mater.* **6**, 679–700 (2020).
- 57 Molesky, S. et al. Inverse design in nanophotonics. *Nat. Photonics* **12**, 659–670 (2018).
- 58 Ozawa, T. et al. Topological photonics. *Rev. Mod. Phys.* **91**, 15006 (2019).
- 59 Saba, M., Hamm, J. M., Baumberg, J. J. & Hess, O. Group theoretical route to deterministic weyl points in chiral photonic lattices. *Phys. Rev. Lett.* **119**, 227401 (2017).
- 60 Chen, P. et al. Quasi-phase-matching-division multiplexing holography in a three-dimensional nonlinear photonic crystal. *Light: Sci. Appl.* **10**, 146 (2021).
- 61 Kadic, M., Milton, G. W., van Hecke, M. & Wegener, M. 3D metamaterials. *Nat. Rev. Phys.* **1**, 198–210 (2019).
- 62 Han, L. & Che, S. An overview of materials with triply periodic minimal surfaces and related geometry: from biological structures to self-assembled systems. *Adv. Mater.* **30**, 1705708–1705729 (2018).
- 63 Dolan, J. A. et al. Optical properties of gyroid structured materials: from photonic crystals to metamaterials. *Adv. Opt. Mater.* **3**, 12–32 (2015).
- 64 Saba, M. et al. Group theory of circular-polarization effects in chiral photonic crystals with four-fold rotation axes applied to the eight-fold intergrowth of gyroid nets. *Phys. Rev. B* **88**, 245116 (2013).

- 65 Wohlgenuth, M., Yufa, N., Hoffman, J. & Thomas, E. L. Triply periodic bicontinuous cubic microdomain morphologies by symmetries. *Macromolecules* **34**, 6083–6089 (2001).
- 66 Prasad, I. et al. Anatomy of triply-periodic network assemblies: characterizing skeletal and inter-domain surface geometry of block copolymer gyroids. *Soft Matter* **14**, 3612–3623 (2018).
- 67 Meade, R. D., Rappe, A. M., Brommer, K. D. & Joannopoulos, J. D. Nature of the photonic band gap: some insights from a field analysis. *J. Opt. Soc. Am. B* **10**, 328–332 (1993).
- 68 He, M. et al. Colloidal diamond. *Nature* **585**, 524–529 (2020).
- 69 Boyd, J. P. Chebyshev & Fourier Spectral Methods. (Springer, 1989).
- 70 Rodriguez, A., Ibanescu, M., Joannopoulos, J. D. & Johnson, S. G. Disorder-immune confinement of light in photonic-crystal cavities. *Opt. Lett.* **30**, 3192–3194 (2005).
- 71 Wang, C. et al. Construction of the single-diamond-structured titania scaffold-recreation of the holy grail photonic structure. *Proc. Natl. Acad. Sci. U.S.A.* **121**, e2318072121 (2024).
- 72 Sheng, Q. et al. Self-assembly of single-diamond-surface networks. *Angew. Chem. Int. Ed.* **60**, 15236–15242 (2021).
- 73 Shin, H. J., Ryoo, R., Liu, Z. & Terasaki, O. Template synthesis of asymmetrically mesostructured platinum networks. *J. Am. Chem. Soc.* **123**, 1246–1247 (2001).
- 74 Akbar, S., Elliott, J. M., Rittman, M. & Squires, A. M. Facile production of ordered 3d platinum nanowire networks with “single diamond” bicontinuous cubic morphology. *Adv. Mater.* **25**, 1160–1164 (2013).
- 75 La, Y. et al. Templated synthesis of cubic crystalline single networks having large open-space lattices by polymer cubosomes. *Nat. Commun.* **9**, 5327–5335 (2018).
- 76 Karpov, D. et al. High-resolution three-dimensional imaging of topological textures in nanoscale single-diamond networks. *Nat. Nanotechnol.* **19**, 1499–1506 (2024).

- 77 Dörr, T. S. et al. Ordered mesoporous tio₂ gyroids: effects of pore architecture and nb-doping on photocatalytic hydrogen evolution under uv and visible irradiation. *Adv. Energy Mater.* **8**, 1802566–1802576 (2018).
- 78 Li, Z. et al. Linking experiment and theory for three-dimensional networked binary metal nanoparticle–triblock terpolymer superstructures. *Nat. Commun.* **5**, 3247–3256 (2014).
- 79 Dong, Q. et al. Inverse design of complex block copolymers for exotic self-assembled structures based on bayesian optimization. *ACS Macro Lett.* **12**, 401–407 (2023).
- 80 Dong, Q. & Li, W. Effect of molecular asymmetry on the formation of asymmetric nanostructures in abc-type block copolymers. *Macromolecules* **54**, 203–213 (2021).
- 81 Deubel, M. et al. Direct laser writing of three-dimensional photonic-crystal templates for telecommunications. *Nat. Mater.* **3**, 444–447 (2004).
- 82 Zhang, W. et al. Printing of 3d photonic crystals in titania with complete bandgap across the visible spectrum. *Nat. Nanotechnol.* **19**, 1813–1820 (2024).
- 83 Turner, M. D. et al. Miniature chiral beamsplitter based on gyroid photonic crystals. *Nat. Photonics* **7**, 801–805 (2013).
- 84 Yang, L. et al. Multi-material multi-photon 3d laser micro- and nanoprinting. *Light: Advanced Manufacturing* **2**, 296–312 (2021).
- 85 Blank, J. & Deb, K. Pymoo: multi-objective optimization in python. *IEEE Access* **8**, 89497–89509 (2020).